Author Manuscript

Author Manuscript

Author Manuscript

Author Manuscript

HHS Public Access

Author manuscript

*J Am Chem Soc*. Author manuscript; available in PMC 2019 April 20.

Published in final edited form as:

*J Am Chem Soc*. 2019 January 09; 141(1): 262–271. doi:10.1021/jacs.8b09311.

# Fluorescence enhancement of a microbial rhodopsin via electronic reprogramming

**María del Carmen Marín**[#†,¶], **Damianos Agathangelou**[#§], **Yoelvis Orozco-Gonzalez**[¶,‡], **Alessio Valentini**[#], **Yoshitaka Kato**[¶¶], **Rei Abe-Yoshizumi**[¶¶,¶¶¶], **Hideki Kandori**[¶¶,¶¶¶], **Ahreum Choi**[§§], **Kwang-Hwan Jung**[§§], **Stefan Haacke**[§], and **Massimo Olivucci**[†,¶,‡]

[†]Biotechnology, Pharmacy and Chemistry Department, University of Siena, Siena, Italy, 53100.

[¶]Chemistry Department, Bowling Green State University, Ohio, 43403.

[§]University of Strasbourg–CNRS, Institute of Physics and Chemistry of Materials of Strasbourg, 67034 Strasbourg, France.

[‡]Université de Strasbourg, USIAS Institut d'Études Avanceés, 67083 Strasbourg, France

[#]Theoretical Physical Chemistry, UR Molsys, University of Liège, Liège, Belgium.

[¶¶]Department of Life Science and Applied Chemistry, Nagoya Institute of Technology, Showa-ku, Nagoya, Japan, 466-8555.

[¶¶¶]OptoBioTechnology Research Center, Nagoya Institute of Technology, Showa-ku, Nagoya, Japan, 466-8555.

[§§]Department of Life Science and Institute of Biological Interfaces, Sogang University, Sogang, South Korea, 04107.

[#] These authors contributed equally to this work.

## Abstract

The engineering of microbial rhodopsins with enhanced fluorescence is of great importance in the expanding field of optogenetics. Here we report the discovery of two mutants (W76S/Y179F and L83Q) of a sensory rhodopsin from the cyanobacterium *Anabaena* PCC7120 with opposite fluorescence behavior. In fact, while W76S/Y179F displays, with respect to the wild-type protein, a nearly ten-fold increase in red-light emission, the second is not emissive. Thus, the W76S/Y179F, L83Q pair offers an unprecedented opportunity for the investigation of fluorescence enhancement in microbial rhodopsins, which is pursued by combining transient absorption spectroscopy and multi-configurational quantum chemistry. The results of such an investigation point to an isomerization-blocking electronic effect as the direct cause of instantaneous (sub-picosecond) fluorescence enhancement.

**Corresponding Author:** molivuc@bgsu.edu., stefan.haacke@ipcms.unistra.fr.

ASSOCIATED CONTENT

**Supporting Information.** Supporting Information text and QM/MM ground state optimized structures of ASR WT, L83Q and W76S/Y179F mutants, in PDB format are provided. The Supporting Information is available free of charge on the ACS Publications website.

The authors declare not competing financial interest.

Author Manuscript Author Manuscript Author Manuscript Author Manuscript

## Graphical Abstract

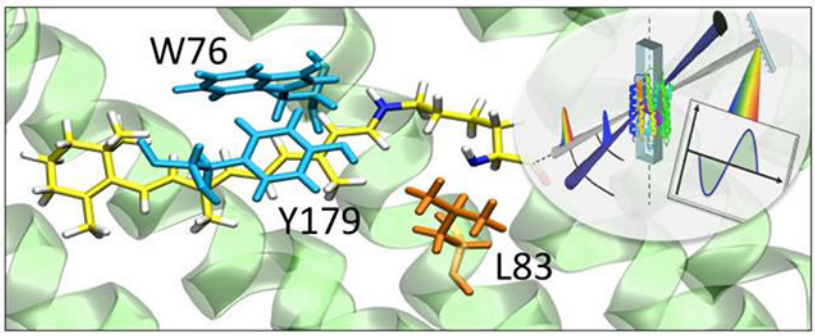


## Introduction

Microbial rhodopsins have been instrumental for the development of optogenetics. In fact, when certain rhodopsins are expressed in neurons, light can be used to activate, inhibit and even visualize neuronal activity.[1] Indeed, few rhodopsins have been reported to exhibit a weak fluorescence,[2–4] a property that is being harnessed to develop superior action potential visualization techniques.[2, 3, 5] The understanding of the factors determining rhodopsin fluorescence is the target of the present work as a high fluorescence intensity is a prerequisite for the development of voltage sensors.[2, 4, 6]

Archaerhodopsin 3 (Arch3)[2] from the dead sea archaebacterium *Halorubrum Sodomense*, is a fluorescent microbial rhodopsin that is currently employed to visualize action potentials in neurons with space and temporal resolution.[5, 7–10] However, its fluorescence is very dim (c.a. 0.001 quantum yield) and three photons must be absorbed to generate one emitted photon. Furthermore, since the emission is not due to the dark adapted (DA) state but to a photocycle intermediate formed only milliseconds after photoexcitation, Arch3 has a limited temporal resolution. Finally, Arch3 proton pumping activity partially silences the action potential signal.[9]

In order to overcome the limitations outlined above, one could look for Arch3 variants [5, 8, 10] or for variants of other microbial rhodopsins[4, 7, 11] displaying enhanced fluorescence intensity. The first approach has yielded, for instance, QuasAr1[8], QuasAr2[8], Archer[7] and Archon1[12] with the first displaying a remarkable 19-fold fluorescence increase generated by a one-photon process. The second approach has instead been applied to a rhodopsin from *Gleobacter violaceous* and yielded a mutant displaying a ca. 0.01 fluorescence quantum yield.[11] A third approach involves the use of cyanine-based chromophore analogues, but it has the disadvantage of not using the natural chromophore[13]. In spite of this progress, obtained through random or systematic mutagenesis, no attempt to unveil the mechanism behind emission enhancement has been reported. As a consequence, our ability to search rationally for highly fluorescent rhodopsins remains impaired.

In the present combined experimental and theoretical study, we consider the second approach by focusing on Anabaena Sensory Rhodopsin (ASR), a light sensor from the fresh water eubacterium *Anabaena*.[14–16] ASR exhibits a dim fluorescence[17] similar to Arch3 but

Author Manuscript Author Manuscript Author Manuscript Author Manuscript

has only a weak (inverse) proton pumping activity. Furthermore, ASR exists in two forms; all-*trans* ASR ($ASR_{AT}$) and 13-*cis* ASR ($ASR_{13C}$), which can be interconverted with light of different wavelengths. Such bistability (i.e. photochromism) is an attractive feature as it provides the basis for engineering photoswitchable fluorescent probes.[18] Finally, the X-ray crystallographic structure of ASR is available,[16] making possible the construction of realistic computer models of both wild type (WT) forms, their isomers and mutants.

Below we report on the accidental discovery of two ASR mutants featuring, with respect to WT, DA states with opposite fluorescence variations. In fact, W76S/Y179F displays an almost one order of magnitude enhanced fluorescence, while L83Q displays a fluorescence slightly larger than the WT but a shorter excited state lifetime (ESL). By using transient absorption spectroscopy (TAS) and quantum mechanics/molecular mechanics (QM/MM) models based on multi-configurational quantum chemistry (MCQC), we show that the ESL and, likely, the fluorescence intensity, is controlled by the changes in the electronic character along the first singlet excited state ($S_1$) potential energy surface (PES) of ASR. Indeed, the models show that the increased mixing between charge transfer and diradical characters along the $S_1$ isomerization path is responsible for the increase in fluorescence of W76S/Y179F. The same models show that the ESL decrease of L83Q, originates from a dramatic decrease of such mixing. The QM/MM model analysis shows that specific electrostatic and steric interactions control the charge transfer/diradical mixing opening a path to the rational engineering of highly fluorescent rhodopsins.

## Methods

### Sample preparation and spectroscopy

ASR proteins were expressed in E. Coli, prepared according to the reported protocol[19] and solubilized in buffer (200mM NaCl, 25 Mm Tris-HCl, 0.02%DDM, pH 7.0). The steady state absorption spectra of the DA and light-adapted (LA) proteins were recorded by using a Perkin Elmer “Lambda 950” UV/VIS spectrometer. DA samples were prepared by incubation in the dark for at least 12 hours at room temperature while the LA samples, orange-adapted (OA) or green-adapted (GA), were exposed to light illumination for 30 min using Luxeon LEDs “LXHL-PL01” (590±10 nm) or “LXHL-NE98” (500±15 nm) respectively.

The fluorescence emission spectra for DA, OA and GA states were recorded by using a home-made static fluorescence setup.[15] Replacement of the excited volume, required for preserving the DA state, was achieved by circulation of the sample, using a peristaltic pump through a close circuit consisting of a 0.5 mm path length flow cell and a 2 mL vial serving as sample reservoir. A Pylon’s nitrogen cooled CCD (−120 ºC, PyLoN, Princeton Instr.) mounted on an imaging spectrometer (SP-2300i, Princeton Instr.) was used for detection of the signal covering the 550–1050 nm spectral range with 4 nm resolution. See the SI for more details.

TAS was carried out with sub-80 fs temporal resolution at 1kHz repetition rate (system described elsewhere[20]). A home-made non-collinear parametric amplifier was used for delivering sub-60 fs excitation pulses at the wavelength of interest while a NIR broad band

Author Manuscript Author Manuscript Author Manuscript Author Manuscript

probe pulse (850–1400 nm) was produced by focusing ~0.7 μJ of the 800 nm fundamental beam in a 4 mm thick YAG crystal.[21] The probe beam was dispersed in an Acton "SP2156" spectrograph and the single pulse spectra at 1kHz were recorded by a Hamamatsu IR head sensor (G11608–256).

Determination of the LA-dependent isomer content was done after retinal oxime extraction, by performing High Performance Liquid Chromatography.[19] Retinal oximes were resolved using a Dionex UltiMate 3000 System, equipped with a Zorbax SIL 70 Å 4.6 × 250 mm – 5 μm Column (see detailed protocol in the SI).

### Computations

The QM/MM models were built using the Automatic Rhodopsin Modeling (ARM) protocol[22] (see Fig. 1A and the SI for details). ARM employs the complete active space self-consistent field (CASSCF)[23] MCQC method combined with the Amber molecular mechanics force field to obtain ground state ($S_0$) QM/MM models of rhodopsins semi-automatically in a standardized fashion. Vertical excitation energies are then computed using multi-configurational second-order perturbation theory (CASPT2)[24] to recover the dynamic electron correlation missing by the CASSCF wave-function.

Excited state reaction paths are documented by computing relaxed scans driven by the $C_{12}$-$C_{13}$=$C_{14}$-$C_{15}$ dihedral angle of the rhodopsin chromophore (Fig. 1E). The $S_1$ dynamics is instead investigated by computing semi-classical Franck-Condon (FC) trajectories, namely deterministic surface-hop trajectories released on $S_1$ PES starting from the $S_0$ equilibrium structure with zero initial velocities. All QM/MM energy, gradient, relaxed scan and FC trajectory calculations were carried out using interfaced Molcas[25] quantum chemistry and Tinker[26] molecular mechanics/dynamics packages.[27]

## Results and Discussion

### Bonding in the excited electronic state

Here we introduce the theoretical framework necessary to discuss the results presented below. Since, a detailed discussion can be found in recent publications,[28, 29] we limit ourselves to a summary of the properties of the first three PESs of a gas-phase model of the rhodopsin chromophore featuring five conjugating double-bonds (PSB5).[17, 29] Scheme 1A shows the electronic characters dominating the $S_0$, $S_1$ and $S_2$ equilibrium structures of PSB5 when this is subject to a planarity constraint. These are labeled 1Ag, 1Bu, and 2Ag (consistent with the electronic terms of a homologous all-*trans* polyene with $C_{2h}$ symmetry).[28, 30] $S_1$ has a 1Bu character characterized by a positive charge spread (i.e. transferred) towards the $H_2C$=CH− end of the PSB5 framework. This is qualitatively different from the 1Ag character of $S_0$ which has the positive charge localized on the −C=$NH_2$ terminal moiety. In contrast, the second singlet excited state ($S_2$) has 2Ag character associated with a diradical, rather than charge transfer, structure and features, similar to $S_0$, with a positive charge mostly located on the −C=$NH_2$ moiety.

In the present work, we take the 1Ag, 1Bu, and 2Ag charge distributions as a reference to follow how the electronic character changes along the $S_1$ PESs (e.g. along a reaction path or

Author Manuscript Author Manuscript Author Manuscript Author Manuscript

trajectory). To do so, we compute the charge of a suitable chromophore moiety and track its variations along the PES. For example, as shown in the right part of Scheme 1A and consistently with the resonance formulas, the −CH−CH−CH−CH−$NH_2$ moiety of has a large positive charge (ca. +0.8) in regions with dominating 1Ag and 2Ag characters but a smaller charge (ca. +0.5) when the 1Bu charge transfer character is dominating. Second, the same charge provides information on the nature of the π-bonding along the path. This is shown in Scheme 1A where we report the bond lengths of the equilibrium reference structures. A structure dominated by a 1Bu character displays inverted double and single bond lengths facilitating double bond isomerization (see values in red). In contrast, in a structure with 2Ag character, the double bonds are only weakened (i.e. partially broken) and thus feature a residual torsional energy barrier restraining double bond isomerization. Third, one can use the charge distribution to track the electronic coupling between two PESs. For instance, the fact that along a trajectory the $S_1$ and $S_2$ charges of the −CH−CH−CH−CH−$NH_2$ moiety change in a mirror-image like fashion,[29, 31] indicates that the $S_1$ and $S_2$ PESs are electronically coupled. In other words, the PESs exchange 1Bu (reactive) and 2Ag (non-reactive) character. This occurs in the presence of an avoided crossing region as the one illustrated in Scheme 1B. In such a scheme, the 1Bu and 2Ag electronic characters are regarded as diabatic states (i.e. states with pure characters), which mix to generate the $S_1$ and $S_2$ adiabatic states. In the left diagram, the $S_2$ and $S_1$ PESs remain dominated by the same diabatic state. In contrast, the right diagram displays a situation where the diabatic states cross twice and, therefore, the $S_1$ PES shows regions dominated by a 2Ag character. The electronic states driving the photoisomerization of model retinal chromophores have originally been described by Josef Michl and Vlasta Bonačić Koutecky.[30, 32]

Below we assume that the ESL is determined by the chromophore $S_1$ reactivity. In other words, the isomerization motion on $S_1$, leading to fast non-radiative decay through a CI between the $S_1$ and $S_0$ PESs, is held responsible for the sub-picosecond ESL and the low fluorescence quantum yield (QY). Consistently, the presence of an energy barrier along the $S_1$ isomerization path would increase the ESL and QY proportionally to the barrier magnitude.

## Spectroscopy and reactivity studies

The observed absorption spectra of the DA, OA and GA states of ASR, are reported in Fig. 2A for the WT and W76S/Y179F and L83Q mutants. As shown in Fig. 2B the observed trend in absorption maxima ($\lambda^a_{max}$) is reproduced by using all-*trans* QM/MM models to compute the corresponding vertical excitation energies for the $S_0 \rightarrow S_1$ transition ($\Delta E_{S1\text{-}S0}$). The blue-shifted $\lambda^a_{max}$ of W76S/Y179F and L83Q (6 and 4 kcal/mol respectively, in terms of $\Delta E_{S1\text{-}S0}$) must originate from changes in the interactions between protein and chromophore (see Fig. 1B to 1D). More specifically, the change from Leucine (L) to Glutamine (Q) in L83Q and the change from Tryptophan (W) to Serine (S) and Tyrosine (Y) to Phenylalanine (F) in W76S/Y179F, must destabilize $S_1$ with respect $S_0$ (or stabilize $S_0$ with respect to $S_1$).

In Fig. 2C we also report the fluorescence spectra of DA WT, L83Q and W76S/Y179F. Also GA and OA spectra are shown for the W76S/Y179F mutant. Experimental spectra are

Author Manuscript Author Manuscript Author Manuscript Author Manuscript

rescaled in order to correct for the sample dependent absorbance values. The integrated fluorescence intensity is thus proportional to the fluorescence QY (see SI). Remarkably, the data show that the QY of W76S/Y179F is ca. one order of magnitude higher than that of WT and, therefore, not far from that of certain improved Arch3 mutants.[7, 8] In Fig. 2B we show that the same all-*trans* QM/MM models reproduce the observed trend in emission maxima ($\lambda^{f}_{max}$). In fact, the $\Delta E_{S1\text{-}S0}$ (see Table S3) computed at the corresponding $S_1$ equilibrium structure (see $MIN_{WT}$ and $MIN_{W76S/Y179F}$ in Fig. 3C and 3E), yield a $\lambda^{f}_{max}$ of 758 nm for WT and 744 nm for W76S/Y179F. However, these values do not account for the kinetic energy of the molecule. To do so, we compute the average $\Delta E_{S1\text{-}S0}$ values along the FC trajectories of Fig. 4C and 4E starting 15 fs after the initial relaxation. The computed $\lambda^{f}_{max}$ of 672 nm for WT and 654 nm for W76S/Y179F, are closer to the observed values of 674 nm for WT and 658 nm for W76S/Y179F.

As displayed in Fig. 2D and Table 1, the ESL values are critically dependent on the mutations, as determined from the stimulated emission (SE) decay traces. We find values of 0.48 ps, 0.86 ps and 5.7 ps for L83Q, WT and W76S/Y179F, respectively (global fit of the entire SE data set, see SI). Comparing W76S/Y179F and WT, the measured and spectrally integrated steady-state emission intensities (see SI for details), are almost proportional to the average ESLs, as expected since the fluorescence QY is $\Phi = ESL*k_r$, with $k_r$ being the radiative rate. L83Q shows a larger QY despite an almost two-fold reduction of the ESL, indicating that L83Q has a higher radiative rate than WT (see SI for details).

A complication arises for W76S/Y179F, which presents a light-adaptation dependent isomer content, including the non-canonical 9-*cis* or 7-*cis* isomers, with a relative amount comparable to all-*trans*. Importantly, in the GA state a relative amount of 54% of the pair 9-*cis* and 7-*cis* isomers accumulates in $S_0$ absorption and was used for comparison with the OA state where the all-trans isomer is the dominant one (39%, see SI). For both the TAS and steady-state fluorescence experiments, the excitation wavelength was tuned to the lower energy tail of ground state absorption for selective excitation of all-*trans* isomer since its $\lambda^{a}_{max}$ was calculated to be largest among all isomers. We find indeed that 9-*cis* and 7-*cis* isomers rather absorb in the 410–420 nm range (see SI). The SE dynamics are identical for both OA and GA light-adaptation states, even though the amount of 9-*cis* and 7-*cis* isomers almost doubles in GA. We thus conclude that in the present conditions, the ESL and the increased fluorescence emission comes mainly from the all-trans isomer.

In the following, we will show that the above all-*trans* QM/MM models reproduce the trends in ESLs and fluorescence intensities when they are probed via reaction paths and 200 fs FC trajectory computations.

The photochemical reactivity of WT, L83Q and W76S/Y179F has been initially investigated by computing the all-*trans* to 13-c*is* relaxed scans connecting the FC point to the $S_1/S_0$ CI along the $C_{13}=C_{14}$ twisting describing the isomerization. The resulting energy profiles are reported in Fig. 3A, 3C and 3E. It is apparent that the steep $S_1$ potential energy profile of L83Q would accelerate the $S_1$ population towards the CI more effectively than the flatter WT and W76S/Y179F PESs. The results appear to be consistent with the measured ESLs, fluorescence intensities and quantum yields (see Table 1 and Figures 2C and D). More

Author Manuscript Author Manuscript Author Manuscript Author Manuscript

specifically, WT and W76S/Y179F display $S_1$ energy profiles (see Fig. 3C and 3E) featuring a ca. 3 and 6 kcal/mol isomerization barriers, respectively, leading to an increased ESL for the double mutant.

The results of 200 fs FC trajectory calculations for the all-*trans* models of L83Q, WT and W76S/Y179F are given in Fig. 4A, 4C and 4E respectively. In all cases, we assume that during such a short time, the trajectories describe the average evolution of population on the lowest excited states ($S_1$ and $S_2$).[35] As shown in Fig. 4A, L83Q reaches the photochemically relevant $S_1/S_0$ CI and decays to $S_0$ in ca. 100 fs consistently with the dominant 270 fs decay (Table 1) as well as the $S_1$ potential energy slope of Fig. 3A (Notice that FC trajectories usually decay earlier with respect to the population investigated experimentally. See Figure 9 in ref. 35) In contrast, Fig. 4C and 4E show that WT and W76S/Y179F do not reach the CI within the simulation time, consistently with the observed shortest decay time which is, in both cases, above 500 fs and with the computed $S_1$ barriers in Figures 3C and E.

The computational results above are based on all-*trans* QM/MM models. Such models do not take into account the effect of mutations on the isomer composition of the DA state which may be altered in the mutants. In fact, as said above, in contrast with WT and L83Q, whose DA states are dominated by the all-*trans* chromophore, W76S/Y179 has a more complex isomer composition (see Figure S11, Table S4). However, as explained above, the OA and GA steady-state absorption together with the isomer compositions for both OA and GA show that the 7-*cis* and 9-*cis* isomers do not contribute to the absorption band at 490 nm. Thus, the presence of these isomers does not alter the conclusions for W76S/Y179 based on the all-*trans* model exclusively.

## Structure and dynamics of the emissive excited state species

In the present sub-section we use the all-*trans* QM/MM models to investigate the mechanisms at the basis of the observed and simulated fluorescence enhancement. More specifically, we provide evidence that the increase in mixing between the reactive 1Bu and non-reactive 2Ag characters introduced above, correlates with the observed L83Q<WT<W76S/Y179F trend in $S_1$ ESL. In other words, we provide support for a structure of the L83Q and W76S/Y179F PESs and related dynamics consistent with the left and right diagram of Scheme 1B respectively.[29]

The comparison of Figures 3A, 3C and 3E shows that the average $S_2$-$S_1$ energy gap along the $S_1$ path decreases in the order L83Q>WT>W76S/Y179F. As apparent from Figures 3B, 3D and 3F such changes are accompanied by changes in the positive charge distribution and, in turn, 1Bu character (see discussion above). Thus, in W76S/Y179F the population moving out of the FC point, where one has a 1Bu character (i.e. the $S_1$ charge of the −CH−CH−CH −CH−$NH_2$ fragment is less than in $S_0$ and $S_2$), transits along regions where the 2Ag character of the $S_1$ PES increases ($MIN_{W76S/Y179F}$ in Figure 3E) indicating character mixing and then reaches regions (ca. −120º in Figure 3F) where the 1Bu and 2Ag characters have close weights (similar charge in $S_1$ and $S_2$). This happens at a lesser extent in WT featuring a larger 1Bu weight in $S_1$ and at an even lesser extent in L83Q where the charge becomes less than +0.2 and the 1Bu character is retained. This appears to be also consistent with the

Author Manuscript Author Manuscript Author Manuscript Author Manuscript

larger $S_2$-$S_1$ gap along the energy profiles of Figure 3C which is brought to a periodic degeneracy (see Figure 4C) only when the chromophore acquires kinetic energy.

The magnitude of the $S_1$ barrier ($E^F$ in Figures 3C and 3E) and, in turn, the ESL, appears to increase with the mixed 1Bu/2Ag character at the ca. −120º twisted structure (see Figures 3B, 3D and 3F) which approximates the $S_1$ transition state. This suggests that, in contrast to L83Q, in W76S/Y179F the $S_1$ and $S_2$ PESs are generated via avoided crossings between 2Ag and 1Bu diabatic states as illustrated in Scheme 1B left. In other words, the $S_1$ energy barrier at −120º would be a result of such crossing.

The increasing 2Ag character along the $S_1$ energy profile in W76S/Y179F must have important consequences on the excited state dynamics. 2Ag being less reactive than 1Bu as demonstrated by the documented $E^F$ barrier, the molecular population will be temporarily trapped in $S_1$ causing an increase in ESL with respect, for instance, to L83Q where the 1Bu character dominates and the $S_1$ PES has no barrier. However, since the reaction paths of Figure 3 do not consider kinetic energy effects, we have confirmed the above conclusion via FC trajectory calculations. Consistently with literature data,[28] initially all trajectories relax along a bond-length-alternation (BLA) stretching mode where the single bonds shrink and the double bonds expand. During BLA relaxation, which occurs within 30 fs, L83Q, WT and W76S/Y179F enter a $S_2/S_1$ near degeneracy region which is associated with the emissive species (sometimes called fluorescent state). Such region shall eventually be left to follow the C13=C14 isomerization coordinate. As anticipated above, we find that only L83Q exits such a region within the 200 fs simulation time supporting the mechanistic interpretation provided by the reaction paths (see Figure 5A).

The FC trajectories provide a detailed dynamic description of the $S_1$ trapping process due to the change in electronic character. In fact, in the reactive L83Q case (Figures 4A and 4B), the $S_2$ energy profile only crosses the $S_1$ energy profile in the 20 to 50 fs time segment and then becomes destabilized. Thus, as shown in Figure 4B, the system remains dominated by a 1Bu reactive character and it is not trapped in $S_1$. However, the trapping occurs in WT and W76S/Y179F (for WT see also our previous report.[29] In these cases, the $S_2$ and $S_1$ profiles cross (or couple) periodically generating “islands” with increased non-reactive 2Ag character. These islands are characterized by BLA oscillations (see also Figure 5 below) which modulate the $S_1$ and $S_2$ gap and the associated 1Bu/2Ag character mixing. This is confirmed by the $S_0 \rightarrow S_1$ oscillator strength progression (Figure S6), showing oscillations of a lower magnitude in WT than in W76S/Y179F. The described behavior is supported by the fact that the $S_2$ and $S_1$ positive charge on the reference $C_{12}$-$C_{13}$=$C_{14}$-$C_{15}$=$NH_2$ fragment display mirror-image variations (see Figures 4D and 4F).[29] As a consequence, due to the change in the corresponding electronic/bonding characters such motion hampers the unlocking of the $C_{13}$=$C_{14}$ double bond and, as a consequence, the reactivity of the $S_1$ chromophore. The frequency and depth of such crossing-recrossing events is larger for W76S/Y179F and this is attributed to the $S_2/S_1$ degeneracy which is already accomplished at the reaction path level (compare Figures 3C and 3E). Consistently, in W76S/Y179F the $S_2$ state becomes more stable than $S_1$ periodically each 30 fs. This does not happen in WT where the $S_2$ state only “touches” the $S_1$ energy profile with about the same frequency.

Author Manuscript Author Manuscript Author Manuscript Author Manuscript

The formation of unreactive “islands” can also be documented structurally. For instance, in Figure 5A we report the evolution along the dihedral angle describing the isomerization of the $C_{13}$=$C_{14}$ double bond. The dihedral reaches the typical −110º value of a CI exclusively for L83Q. On the other hand, the generation of unlocked double bonds prone to isomerize (i.e. via double-bond-single-bond inversion) can be tracked by plotting the BLA value of specific chromophore fragment. Accordingly, in Figures 5B–5D we report the evolution of the BLA value of a suitable β-ionone containing fragment. It oscillates about a completely inverted BLA value in L83Q (i.e. negative average BLA values) but not in WT and W76S/Y179F (i.e. positive average BLA values). As mentioned above, the DA state of the fluorescent ASR mutant W76S/Y179F is not dominated by a single all-*trans* isomer which, in fact, only accounts for 30% of the total population. Such state also contains 15% of 13-*cis* and 18% of 11-*cis* isomers and 36% of a mixture of 9-*cis* and 7-*cis* isomers (see Table S4). As said above, the latter can be disregarded since they are not excited in both the steady-state fluorescence and TAS experiments (see SI), but the contribution of 13-*cis* and 11-*cis* isomers needs to be discussed. We have used the same type of QM/MM model to investigate their photoisomerization dynamics via FC trajectory calculations. As shown in Figure S9, the 13-*cis* and 11-*cis* isomer reach a CI within 200 fs, a component which is not observed in the SE decay since the pump wavelength favors all-*trans* excitation. Since, the fluorescence spectra were recorded with the same excitation wavelength, and the increase in fluorescence quantum yield matches the ESL increase of W76S/Y179F with respect to WT, we conclude that these isomers do not contribute to the observed fluorescence. On the other hand, the 9-*cis* and, most likely, the 7-*cis* isomers would contribute with the same mechanism of the all-*trans* isomer (see the SI).

However, again, the steady state absorption spectra of OA and GA states strongly suggest that both isomers absorb in the region between 350–400 nm, are not excited and as a following not presented in the TAS and Static fluorescence measurements (see SI).

## Residue-level modulation of excited state emission

We now provide information on how emissive PES regions (i.e. the islands described above) get stabilized (or destabilized) via electrostatic and/or steric interactions with specific residues. The L83Q, WT and W76S/Y179F models indicate that the increase in ESL is due to the appearance of an $S_1$ energy barrier at ca. −120º twisting whose magnitude increases with the 1Bu/2Ag mixing developing along the $S_1$ PES. On the other hand, it is unclear if such variations are caused by changes in the electrostatic field acting on the chromophore or by changes in the chromophore geometrical progression (i.e. in the isomerization coordinate). To investigate the electrostatic effect we recomputed the energy profile of Figure 3A (i.e. for L83Q) for the isolated (i.e. *in vacuo*) chromophore taken with its protein geometry. The comparison between Figure 6A and Figure 3A (or the dashed lines in Figure 6A) demonstrates that the change in protein electrostatics is fully responsible for the absence of a barrier in L83Q. Indeed, in the absence of protein electrostatic effects, the energy profile of L83Q appears to be very similar to the one detected along the WT and W76S/Y179F $S_1$ PESs when the protein is present. This behavior must be connected with the charge evolution of Figure 6B which shows a marked difference when plotted in the presence and

Author Manuscript Author Manuscript Author Manuscript Author Manuscript

absence of the protein. In fact, it can be seen that between −140º and −120º the $S_1$ charge evolution displays a fast increase of 1Bu/2Ag mixed character in the isolated chromophore.

Remarkably, the same L83Q barrier induction effect is seen in the presence of a protein environment where the charges of the Q residue in position 83 are set to zero (see Figure S4). This is also consistent with the fact that it is sufficient to replace the polar Q residue with the apolar L residue (or with a "residue" with zero charges) to create the barrier akin to $ASR_{AT}$ which may, in part, be due to the relocation of the remaining cavity charges.

The removal of the $S_1$ barrier at the −120º twisted transition state can thus be directly connected to the interaction between the chromophore orientation, its torsion-induced charge translocation and the Q83 side chain. While, we cannot presently provide a quantitative analysis, our computations reveal two effects. First (see Figure 7A), there is an evident reorientation of the π-conjugated chain along the reaction path and the side-chain of the Q83 residue (compare the torsional deformation of the left structure corresponding to the second point along the path of Figure 3A with the "transition state" structure featuring a −120º twisted $C_{13}$=$C_{14}$ double bond). Second (see Figure 7B), the charge transfer character is increasing along the path thereby enhancing the intensity of the interaction between chromophore and the dipolar Q83 side-chain. Our results suggest that, in presence of the Q83 side-chain charges, the "transition state structure" get stabilized on $S_1$ with respect to the earlier structures along the path and this leads to the disappearance of the $S_1$ barrier. However, such electrostatic stabilization is not an obvious effect as it depends on the exact reorientation of the chromophore during the isomerization and on the change in 1Bu character.

In Figures 6C–6E we report the same *in vacuo* analysis for WT and W76S/Y179F. Remarkably, in both cases there are no qualitative changes in the energy profiles indicating that the $S_1$ barrier is not associated to electrostatic interaction but it is an intrinsic feature of the chromophore geometrical changes along the two paths. This conclusion is also valid for the $S_2/S_1$ degeneracy region of W76S/Y179F which is maintained after removal of the protein electrostatic field. Furthermore, as we show in the SI, it is possible to transform the WT $S_2$, $S_1$ and $S_0$ energy profiles into W76S/Y179F-like energy profiles by simply changing the backbone dihedral angles along the WT reaction coordinate to the corresponding W76S/Y179F values. This is remarkable because those are limited changes which indicate that the fluorescent tuning in rhodopsins might be achieved also through subtle geometrical effects.

## Conclusions

Above we have looked at the origin of experimentally observed fluorescence QY and ESL variations in the DA state of ASR. While mutants of other microbial rhodopsins (e.g. bacteriorhodopsin and proteorhodopsin)[36] display an ESL increase, in our study we have reported on an electronic state mixing mechanism for ESL and fluorescence QY enhancement. In order to do so, the stationary and transient spectral parameters for WT and for L83Q and W76S/Y179 have been measured. Remarkably, while both mutants display, with respect to WT, blue shifted absorption maxima, the measurements reveal opposite ESL changes. Indeed, while it is found that the W76S/Y179F mutant has a picosecond lifetime

Author Manuscript Author Manuscript Author Manuscript Author Manuscript

with a fluorescence QY not too far from the improved Arch3 mutants applied in optogenetics, L83Q fluoresces very weakly and undergoes all-*trans* to 13-*cis* isomerization on a ca. 200 fs timescale.

By using the $ASR_{AT}$ isomer as a DA state model, we show that MCQC-based QM/MM models are capable to reproduce the observed trends in absorption, emission as well as ESL indicating their suitability for mechanistic studies. Accordingly, reaction path and trajectory computations show, consistently, that the observed change in ESL is due to an opposite change in charge transfer character of the $S_1$ state of the molecule. Such changes, that can be described as an increase in unreactive 2Ag diradical character along the L83Q, WT, W76S/Y179F series, do not regard the FC region but a critical segment of the reaction path or trajectory where the rhodopsin chromophore is significantly twisted. This mechanism is different from others that have been proposed for ESL increase in microbial rhodopsins[37]. Notice that a 2Ag/1Bu degeneracy has been reported for the retinal chromophore in solution in both computational[38] and experimental[39] studies.

While the nature of the electronic character variation causing the fluorescence enhancement is found to be consistently the same, QM/MM model analysis points to very different residue-level mechanisms responsible for such variations. In other words, the residue replacements in L83Q and W76S/Y179F appears to operate via dramatically different effects. The L83Q to WT variation is dominated by an electrostatic effect while the WT to W76S/Y179F variation is controlled by steric effects: a change in the details of the isomerization coordinate.

Even if two mutants form a limited set, the consistency of the experimentally observed and simulated quantities confer a high significance to the described findings, which have a direct impact in the design of highly fluorescent rhodopsins. The most significant of these finding is the undeniable intrinsic complexity of the regulation of a basic spectroscopic property such as light emission. In the presented examples, such complexity shows up dramatically even upon a one-two residue replacements and discourages the extraction of simple “rules-of-thumb” which are sometimes introduced, in our opinion inappropriately, in the context of color tuning. On the other hand, our study suggests that the extension of the present study to an entire array of mutants, may reveal if a rapidly computable structure such as the −120º TS located above, and the actual $S_1/S_2$ degree of mixing, can be used for practical *in silico* screening of fluorescent mutants.

As stressed above, the increase in ESL is a factor necessary for employing rhodopsins as fluorescence reporters. Another factor is the sensitivity to voltage changes across the membrane. While a robust study of voltage sensitivity of the $ASR_{AT}$ W76S/Y179F mutant goes beyond the scope of the present work, in the SI we report the result of a preliminary computational investigation. In such study we have probed the sensitivity of the $\lambda^{f}_{max}$ and oscillator strength values of the $ASR_{AT}$ W76S/Y179F QM/MM model to an increase/decrease in the number of external ions in the inner/outer surfaces of the protein (see Figure 1A). The result indicates that the $\lambda^{f}_{max}$ is sensitive to the change in external ion concentration which is assumed to provide a suitable model for voltage variation. Accordingly, $ASR_{AT}$ W76S/Y179F or its variants may lead to promising voltage reporters

Author Manuscript Author Manuscript Author Manuscript Author Manuscript

for observing either the change in fluorescence intensity at a specific wavelength or the change in $\lambda^{f}_{max}$ as a function of time.

## Supplementary Material

Refer to Web version on PubMed Central for supplementary material.

## ACKNOWLEDGMENT

The research has been supported by the following grants NSF CHE-CLP-1710191 and NIH GM126627 01. MO is grateful for a USIAS 2015 grant. HK is grateful for support from MEXT (Japan) and CREST-JST (Japan). KHJ is grateful for grant NRF-2016R1A6A3A11934084 (South Korea). We thank Dr. Luca De Vico for technical help with the computations and for valuable discussions. We thank Mr. Shinya Sugita and Ms. Aki Nemoto for their help with sample preparation.

Funding Sources

USIAS (University of Strasbourg), NSF, NIH, MEXT, CREST-JST, NRF.

## REFERENCES

(1). Berndt A; Lee SY; Ramakrishnan C; Deisseroth K Structure-guided transformation of channelrhodopsin into a light-activated chloride channel. Science 2014, 344, 420–424. [PubMed: 24763591]

(2). Kralj JM; Douglass AD; Hochbaum DR; Maclaurin D; Cohen AE Optical recording of action potentials in mammalian neurons using a microbial rhodopsin. Nat. Methods 2012, 9, 90–95.

(3). Gong Y; Wagner MJ; Li JZ; Schnitzer MJ Imaging neural spiking in brain tissue using FRET-opsin protein voltage sensors. Nat. Commun 2014, 5, 3674. [PubMed: 24755708]

(4). Kralj JM; Hochbaum DR; Douglass AD; Cohen AE Electrical Spiking in Escherichia coli Probed with a Fluorescent Voltage-Indicating Protein. Science 2011, 333, 345–348. [PubMed: 21764748]

(5). Gong Y; Li JZ; Schnitzer MJ Enhanced Archaerhodopsin Fluorescent Protein Voltage Indicators. PLoS ONE 2013, 8, e66959. [PubMed: 23840563]

(6). Looger LL; Griesbeck O Genetically encoded neural activity indicators. Current opinion in neurobiology 2012, 22, 18–23.; [PubMed: 22104761] Looger LL Running in reverse: rhodopsins sense voltage. Nat. Methods 2012, 9, 43.;Mutoh H; Akemann W; Knöpfel T Genetically engineered fluorescent voltage reporters. ACS chemical neuroscience 2012, 3, 585–592.; [PubMed: 22896802] McIsaac RS; Engqvist MKM; Wannier T; Rosenthal AZ; Herwig L; Flytzanis NC; Imasheva ES; Lanyi JK; Balashov SP; Gradinaru V; Arnold FH Directed evolution of a far-red fluorescent rhodopsin. Proc. Natl. Acad. Sci. U. S. A 2014, 111, 13034–13039. [PubMed: 25157169]

(7). Flytzanis NC; Bedbrook CN; Chiu H; Engqvist MKM; Xiao C; Chan KY; Sternberg PW; Arnold FH; Gradinaru V Archaerhodopsin variants with enhanced voltage-sensitive fluorescence in mammalian and Caenorhabditis elegans neurons. Nat. Commun 2014, 5, 4894. [PubMed: 25222271]

(8). Hochbaum DR; Zhao Y; Farhi SL; Klapoetke N; Werley CA; Kapoor V; Zou P; Kralj JM; Maclaurin D; Smedemark-Margulies N; Saulnier JL; Boulting GL; Straub C; Cho YK; Melkonian M; Wong GK-S; Harrison DJ; Murthy VN; Sabatini BL; Boyden ES; Campbell RE; Cohen AE All-optical electrophysiology in mammalian neurons using engineered microbial rhodopsins. Nat. Methods 2014, 11, 825–833. [PubMed: 24952910]

(9). Maclaurin D; Venkatachalam V; Lee H; Cohen AE Mechanism of voltage-sensitive fluorescence in a microbial rhodopsin. Proc. Natl. Acad. Sci. U. S. A 2013, 110, 5939–5944. [PubMed: 23530193]

(10). Hou JH; Venkatachalam V; Cohen AE Temporal Dynamics of Microbial Rhodopsin Fluorescence Reports Absolute Membrane Voltage. Biophys. J 2014, 106, 639–648. [PubMed: 24507604]

Author Manuscript Author Manuscript Author Manuscript Author Manuscript

(11). Engqvist MKM; McIsaac RS; Dollinger P; Flytzanis NC; Abrams M; Schor S; Arnold FH Directed Evolution of Gloeobacter violaceus Rhodopsin Spectral Properties. J. Mol. Biol 2014, 427, 205–220. [PubMed: 24979679]

(12). Piatkevich KD; Jung EE; Straub C; Linghu C; Park D; Suk H-J; Hochbaum DR; Goodwin D; Pnevmatikakis E; Pak N A robotic multidimensional directed evolution approach applied to fluorescent voltage reporters. Nature chemical biology 2018, 14, 352. [PubMed: 29483642]

(13). Herwig L; Rice AJ; Bedbrook CN; Zhang RK; Lignell A; Cahn JKB; Renata H; Dodani SC; Cho I; Cai L; Gradinaru V; Arnold FH Directed Evolution of a Bright Near-Infrared Fluorescent Rhodopsin Using a Synthetic Chromophore. Cell Chem Biol 2017, 24, 415–425.; [PubMed: 28262559] Hontani Y; Ganapathy S; Frehan S; Kloz M; DeGrip WJ; Kennis JTM Strong pH-Dependent Near-Infrared Fluorescence in a Microbial Rhodopsin Reconstituted with a Red-Shifting Retinal Analogue. The journal of physical chemistry letters 2018,

(14). Kawanabe A; Furutani Y; Jung KH; Kandori H Photochromism of Anabaena sensory rhodopsin. J. Am. Chem. Soc 2007, 129, 8644–8649. [PubMed: 17569538]

(15). Cheminal A; Léonard J; Kim SY; Jung K-H; Kandori H; Haacke S Steady state emission of the fluorescent intermediate of Anabaena Sensory Rhodopsin as a function of light adaptation conditions. Chem. Phys. Lett 2013, 587, 75–80.

(16). Vogeley L; Sineshchekov OA; Trivedi VD; Sasaki J; Spudich JL; Luecke H Anabaena sensory rhodopsin: a photochromic color sensor at 2.0 A. Science 2004, 306, 1390–1393. [PubMed: 15459346]

(17). Luk HL; Melaccio F; Rinaldi S; Gozem S; Olivucci M Molecular bases for the selection of the chromophore of animal rhodopsins. Proc. Natl. Acad. Sci. U. S. A 2015, 112, 15297–15302. [PubMed: 26607446]

(18). Mcisaac RS; Bedbrook CN; Arnold FH Recent Advances in Engineering Microbial Rhodopsins for Optogenetics. Curr. Opin. Struct. Biol 2015, 33, 8–15.; [PubMed: 26038227] Deisseroth K Optogenetics. Nat. Methods 2011, 8, 26–29. [PubMed: 21191368]

(19). Jung K-H; Trivedi VD; Spudich JL Demonstration of a sensory rhodopsin in eubacteria: Sensory rhodopsin in eubacteria. Mol. Microbiol 2003, 47, 1513–1522.; [PubMed: 12622809] Choi AR; Kim SY; Yoon SR; Bae K; Jung K-H Substitution of Pro206 and Ser86 residues in the retinal binding pocket of Anabaena sensory rhodopsin is not sufficient for proton pumping function. J. Microbiol. Biotechnol 2007, 17, 138–145. [PubMed: 18051365]

(20). Gueye M; Nillon J; Crégut O; Léonard J Broadband UV-Vis vibrational coherence spectrometer based on a hollow fiber compressor. Rev. Sci. Instrum 2016, 87, 093109. [PubMed: 27782548]

(21). Bradler M; Baum P; Riedle E Femtosecond continuum generation in bulk laser host materials with sub-μJ pump pulses. Appl. Phys. B 2009, 97, 561–574.

(22). Melaccio F; del Carmen Marín M; Valentini A; Montisci F; Rinaldi S; Cherubini M; Yang X; Kato Y; Stenrup M; Orozco-Gonzalez Y; Ferré N; Luk HL; Kandori H; Olivucci M Toward Automatic Rhodopsin Modeling as a Tool for High-Throughput Computational Photobiology. J. Chem. Theory Comput 2016, 12, 6020–6034. [PubMed: 27779842]

(23). Roos BO In Ab Initio Methods in Quantum Chemistry II; Lawley KP, Ed.; Wiley & Sons: Chincester, 1987; pp 399–445.

(24). Andersson K; Malmqvist PA; Roos BO; Sadlej AJ; Wolinski K Second-order perturbation theory with a CASSCF reference function. J. Phys. Chem 1990, 94, 5483–5488.

(25). Aquilante F; Autschbach J; Carlson RK; Chibotaru LF; Delcey MG; De Vico L; Fernandez Galván I; Ferré N; Frutos LM; Gagliardi L; Garavelli M; Giussani A; Hoyer CE; Li Manni G; Lischka H; Ma D; Malmqvist P-Å; Müller T; Nenov A; Olivucci M; Pedersen TB; Peng D; Plasser F; Pritchard B; Reiher M; Rivalta I; Schapiro I; Segarra-Martì J; Stenrup M; Truhlar DG; Ungur L; Valentini A; Vancoillie S; Veryazov V; Vysotskiy VP; Weingart O; Zapata F; Lindh R Molcas 8: New capabilities for multiconfigurational quantum chemical calculations across the periodic table. J. Comput. Chem 2016, 37, 506–541. [PubMed: 26561362]

(26). Ponder JW; Richards FM An efficient newton-like method for molecular mechanics energy minimization of large molecules. J. Comput. Chem 1987, 8, 1016–1024.

(27). Ferré N; Olivucci M Probing the Rhodopsin Cavity with Reduced Retinal Models at the CASPT2//CASSCF/AMBER Level of Theory. J. Am. Chem. Soc 2003, 125, 6868–6869.;

Author Manuscript Author Manuscript Author Manuscript Author Manuscript

[PubMed: 12783530] Ferré N; Cembran A; Garavelli M; Olivucci M Complete-active-space self-consistent-field/Amber parameterization of the Lys296-retinal-Glu113 rhodopsin chromophore-counterion system. Theo. Chem. Acc 2004, 112, 335–341.

(28). Gozem S; Luk HL; Schapiro I; Olivucci M Theory and Simulation of the Ultrafast Double-Bond Isomerization of Biological Chromophores. Chem. Rev 2017, 117, 13502–13565. [PubMed: 29083892]

(29). Manathunga M; Yang X; Orozco-Gonzalez Y; Olivucci M Impact of Electronic State Mixing on the Photoisomerization Timescale of the Retinal Chromophore. J. Phys. Chem. Lett 2017, 8, 5222–5227. [PubMed: 28981285]

(30). Michl J; Bonačić-Koutecký V Electronic aspects of organic photochemistry; Wiley: New York, 1990.

(31). Manathunga M; Yang X; Olivucci M Electronic State Mixing Controls the Photoreactivity of a Rhodopsin with All-trans Chromophore Analogues. J. Phys. Chem. Lett 2018, 9, 6350–6355. [PubMed: 30336038]

(32). Bonačić-Koutecký V; Schöffel K; Michl J Critically heterosymmetric biradicaloid geometries of of protonated Schiff bases. Theor. Chim. Acta 1987, 72, 459–474.

(33). Agathangelou D; Orozco-Gonzalez Y; del Carmen Marín M; Roy PP; Brazard J; Kandori H; Jung K-H; Léonard J; Buckup T; Ferré N; Olivucci M; Haacke S Effect of point mutations on the ultrafast photo-isomerization of Anabaena sensory rhodopsin. Faraday Discuss. 2018, 207, 55–75. [PubMed: 29388996]

(34). Kouyama T; Kinosita K; Ikegami A Excited-state dynamics of bacteriorhodopsin. Biophys. J 1985, 47, 43–54. [PubMed: 3978189]

(35). Manathunga M; Yang X; Luk HL; Gozem S; Frutos LM; Valentini A; Ferré N; Olivucci M Probing the Photodynamics of Rhodopsins with Reduced Retinal Chromophores. J. Chem. Theory Comput 2016, 12, 839–850. [PubMed: 26640959]

(36). Song L; El-Sayed MA; Lanyi JK Protein catalysis of the retinal subpicosecond photoisomerization in the primary process of bacteriorhodopsin photosynthesis. Science 1993, 261, 891–894.; [PubMed: 17783735] Kennis JTM; Larsen DS; Ohta K; Facciotti MT; Glaeser RM; Fleming GR Ultrafast protein dynamics of bacteriorhodopsin probed by photon echo and transient absorption spectroscopy. The Journal of Physical Chemistry B 2002, 106, 6067–6080.;Van Stokkum IHM; Gobets B; Gensch T; van Mourik F; Hellingwerf KJ; van Grondelle R; Kennis JTM (Sub)-picosecond spectral evolution of fluorescence in photoactive proteins studied with a synchroscan streak camera system. Photochem. Photobiol 2006, 82, 380–388. [PubMed: 16613489]

(37). Tahara S; Takeuchi S; Abe-Yoshizumi R; Inoue K; Ohtani H; Kandori H; Tahara T Origin of the Reactive and Nonreactive Excited States in the Primary Reaction of Rhodopsins: pH Dependence of Femtosecond Absorption of Light-Driven Sodium Ion Pump Rhodopsin KR2. The Journal of Physical Chemistry B 2018, 122, 4784–4792.; [PubMed: 29708342] Hontani Y; Marazzi M; Stehfest K; Mathes T; Stokkum IHM; Elstner M; Hegemann P; Kennis JTM Reaction dynamics of the chimeric channelrhodopsin C1C2. Sci. Rep 2017, 7, 7217.; [PubMed: 28775289] Dokukina I; Weingart O Spectral properties and isomerisation path of retinal in C1C2 channelrhodopsin. Phys. Chem. Chem. Phys 2015,

(38). Muñoz-Losa A; Fdez Galván I; Aguilar MA; Martín ME Retinal models: comparison of electronic absorption spectra in the gas phase and in methanol solution. J. Phys. Chem. B 2008, 112, 8815–8823.; [PubMed: 18590305] Demoulin B; Altavilla SF; Rivalta I; Garavelli M Fine Tuning of Retinal Photoinduced Decay in Solution. J. Phys. Chem. Lett 2017, 4407–4412.; [PubMed: 28853582] Munoz-Losa A; Ignacio I; Aguilar MA; Martín ME Simultaneous Solvent and Counterion Effects on the Absorption Properties of a Model of the Rhodopsin Chromophore. J. Chem. Theory Comput 2013, 9, 1548–1556. [PubMed: 26587616]

(39). Nielsen IB; Lammich L; Andersen LH S1 andS2 Excited States of Gas-Phase Schiff-Base Retinal Chromophores. Phys. Rev. Lett 2006, 96, 018304. [PubMed: 16486529]

Author Manuscript Author Manuscript Author Manuscript Author Manuscript

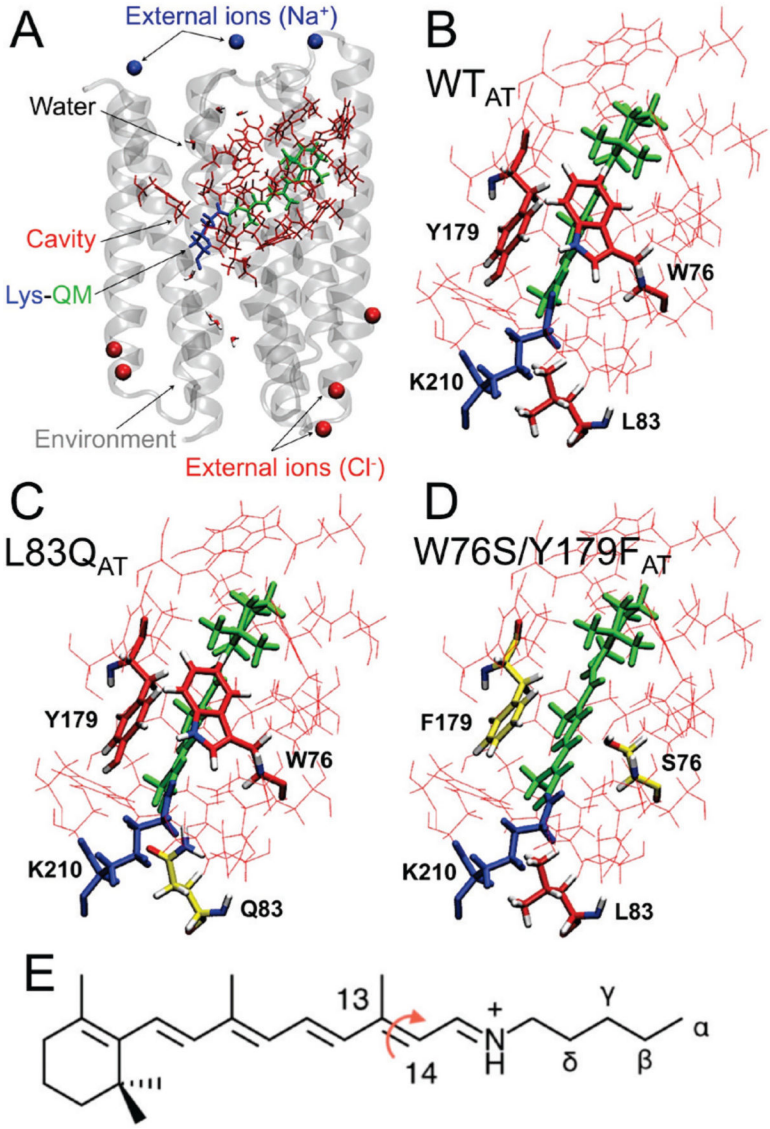


**Figure 1.**

QM/MM models. (A) General structure of the ASR model. The protein environment is colored in grey with external counterions in blue ($Na^+$) and red ($Cl^-$). The region hosting the retinal chromophore is colored in red with the Lys210-chromophore system in blue-green. Chromophore hosting region for the all-*trans* isomers of WT ($ASR_{AT}$), L83Q and W76S/Y179F are given in part (B), (C) and (D) respectively. The variable cavity residues 76, 83 and 179 are shown in tube representation. (E) The all-*trans* retinal chromophore. The curly arrow indicates the $C_{13}$=$C_{14}$ isomerizing double bond and the greek letters the atoms of the Lys210 side chain.

Author Manuscript Author Manuscript Author Manuscript Author Manuscript

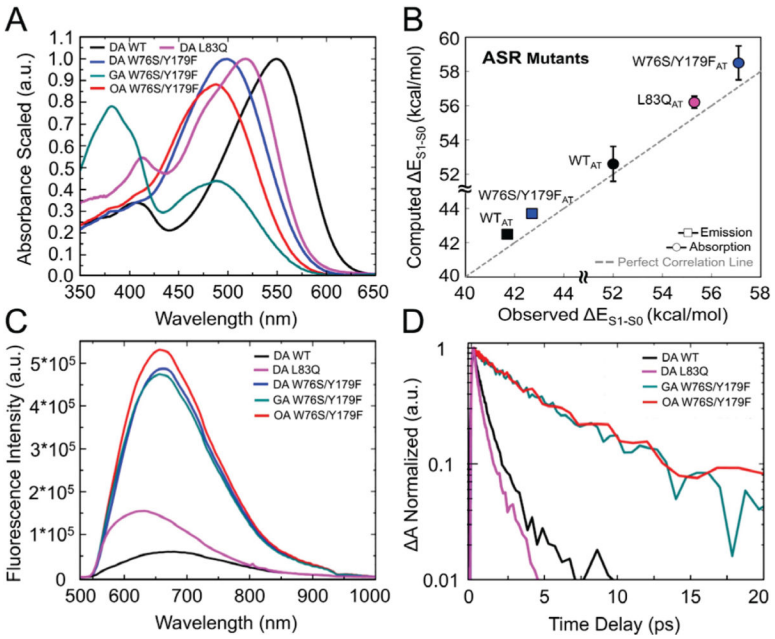


**Figure 2.**

Steady state spectra and excited states dynamics. (A) Scaled absorption spectra of light-adapted (OA and GA) W76S/Y179F mutant and dark-adapted (DA)WT, W76S/Y179F and L83Q mutants of ASR. Light-adaptation was carried out either with an orange or green LED. (B) Comparison between simulated all-*trans* and observed $\lambda^{a}_{max}$ (circles) and $\lambda^{f}_{max}$ (squares) values for the DA state. Deviation bars for the computed excitation energy values are shown as black segments. The excitation energy errors fall in the 0.5–1.5 kcal/mol range typical of ARM[22]. (C) Steady state emission of DA WT ASR, DA L83Q ASR, DA, OA and GA W76S/Y179F mutant of ASR. (D) Comparison of the SE kinetic traces of WT (black trace), L83Q (pink trace) and W76S/Y179F (GA green trace and OA red trace).

Author Manuscript Author Manuscript Author Manuscript Author Manuscript

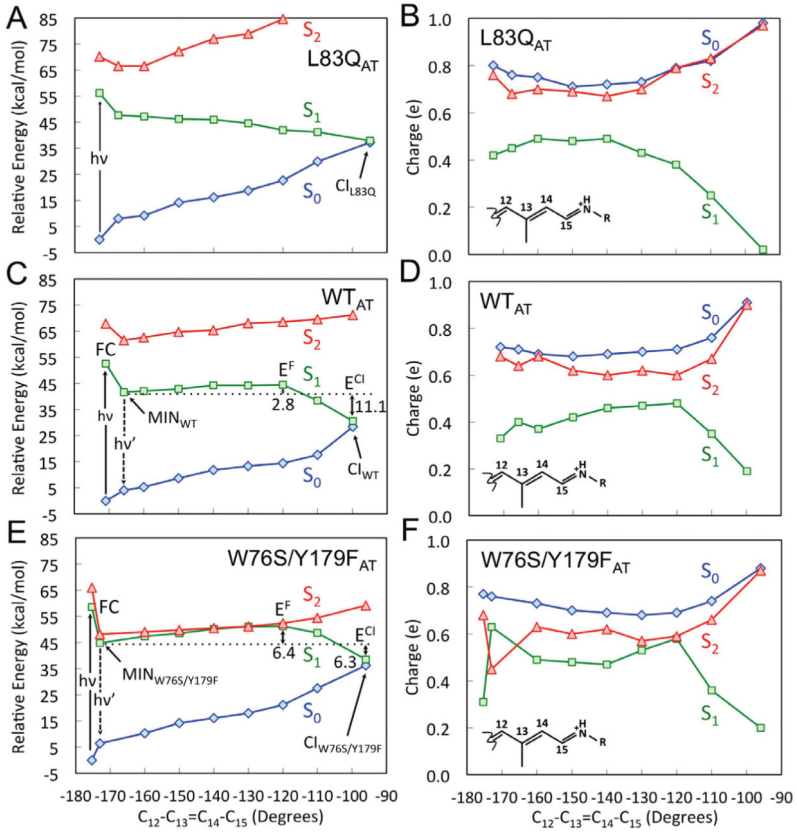


**Figure 3.**

$C_{13}$=$C_{14}$ isomerization path on $S_1$. (A), (C) and (E) CASPT2//CASSCF/AMBER energy profiles along $S_1$ (green squares) isomerization path of L83Q, WT and W76S/Y179F respectively. $S_0$ (blue diamonds) and $S_2$ (red triangles) profiles along the $S_1$ path are also given. The $S_1$ is computed in terms of a relaxed scan along $C_{12}$-$C_{13}$=$C_{14}$-$C_{15}$ dihedral angle. The corresponding, computed oscillator strengths are given in Figure S3. (B), (D) and (F) corresponding Mulliken charge variation of the −CH−CH−CH−CH−$NH_2$ moiety of the chromophore of L83Q, WT and W76S/Y179F respectively.

Author Manuscript Author Manuscript Author Manuscript Author Manuscript

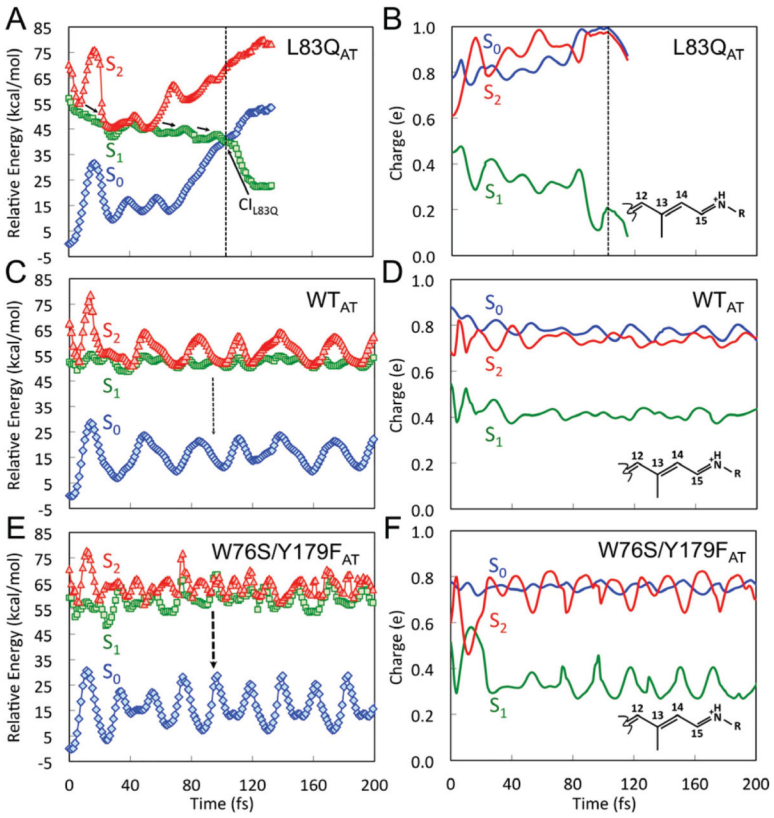


**Figure 4.**

Trajectory computation on $S_1$. (A), (C) and (E) QM/MM FC trajectories (see main text) of L83Q, WT and W76S/Y179F, computed at two-root state-averaged-CASSCF/AMBER level of theory and corrected at the CASPT2 level. $S_0$ (blue diamonds), $S_1$ (green squares) and $S_2$ (red triangles) CASPT2/CASSCF/AMBER energy profiles along the FC trajectories. The corresponding, computed oscillator strengths are given in Figure S6. (B), (D) and (F) corresponding Mulliken charge variation of the −CH−CH−CH−CH−$NH_2$ moiety of the chromophore of L83Q, WT and W76S/Y179F respectively. To test the robustness of the W76S/Y179F results the data of panel E and F have been recomputed at the 5-root-state-average level (see Figure S10).

Author Manuscript Author Manuscript Author Manuscript Author Manuscript

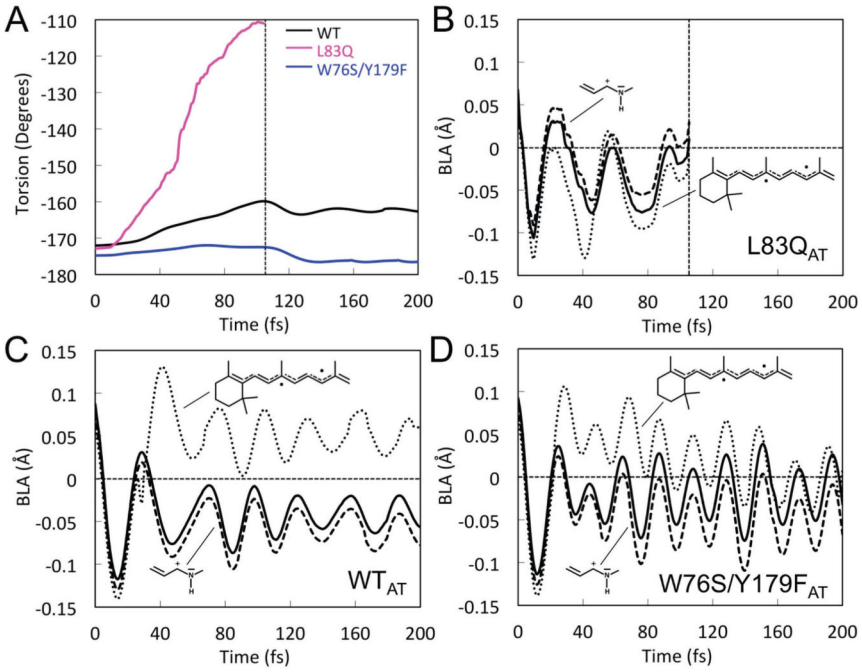


**Figure 5.**

Geometrical variation along the L83Q, WT and W76S/Y179F FC trajectories. (A) Evolution of the $C_{12}$-$C_{13}$=$C_{14}$-$C_{15}$ dihedral angle along the FC trajectories of all-*trans* ASR L83Q (purple), WT (black) and W76S/Y179F (blue) representing the $C_{13}$=$C_{14}$ isomerization. (B), (C) and (D) evolution of the total BLA (full line) and of the BLA of two specific moieties (dotted and dashed lines) for L83Q, WT and W76S/Y179F respectively.

Author Manuscript Author Manuscript Author Manuscript Author Manuscript

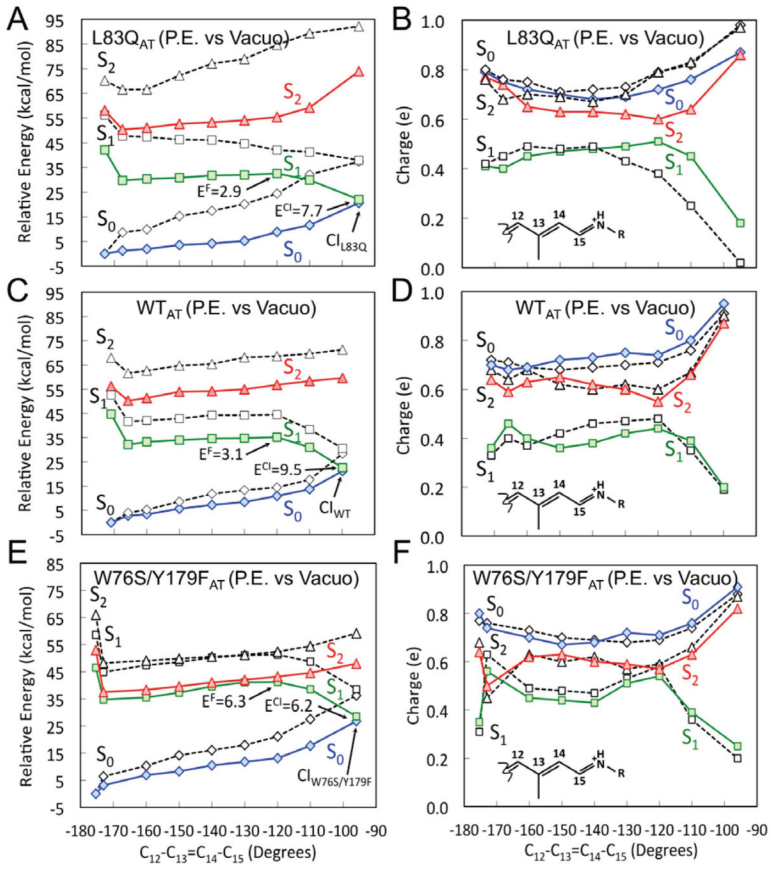


**Figure 6.**

Energy profiles along the $S_1$ isomerization paths of Figure 3 for the chromophore *in vacuo*. (A), (C) and (E) CASPT2//CASSCF/AMBER energy profiles for the $S_1$ state (green squares) of L83Q, WT and W76S/Y179F respectively. $S_0$ (blue diamonds) and $S_2$ (red triangles) profiles along the same path. (B), (D) and (F) corresponding Mulliken charge variation of the −CH−CH−CH−CH−$NH_2$ moiety of the chromophore of L83Q, WT and W76S/Y179F respectively. In all panels the dashed energy profiles represent the corresponding energy profiles of the entire protein models (i.e. from Figure 3).

Author Manuscript Author Manuscript Author Manuscript Author Manuscript

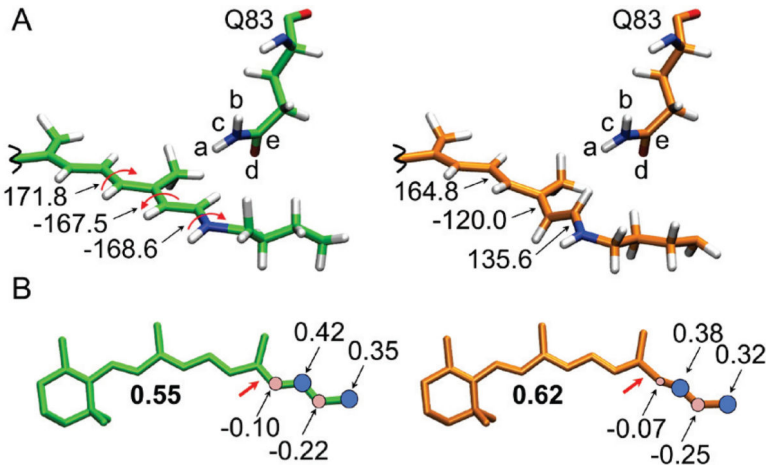


**Figure 7.**

Geometrical and charge distribution variations along the $S_1$ isomerization path of L83Q (see Figure 3A). (A) Geometrical variation documented by three critical dihedral angles (curly arrows). The left structure corresponds to the second point along the energy profile of Figure 3A (i.e. the point corresponding to $MIN_{WT}$ and $MIN_{W76S/Y179}$) while the right structure is the "transition state" structure featuring a −120º $C_{12}$-$C_{13}$=$C_{14}$-$C_{15}$ dihedral angle. (B) Charge distribution data for the same two structures.

Author Manuscript Author Manuscript Author Manuscript Author Manuscript

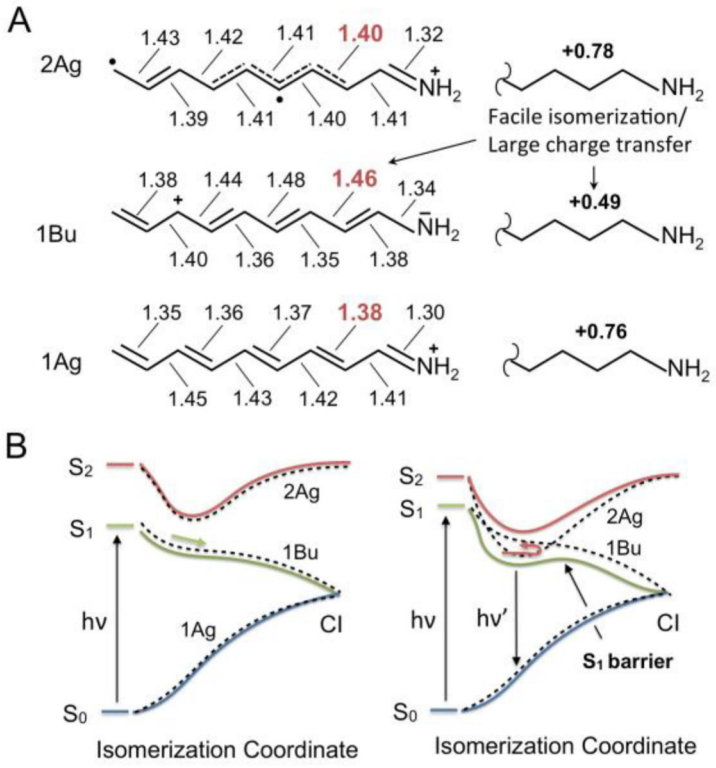


**Scheme 1.**

Electronic and bonding structure of the retinal chromophore. (A) Left. Resonance formula associated to the electronic characters (1Ag, 1Bu and 2Ag) dominating the $S_0$, $S_1$ and $S_2$ equilibrium structures of PSB5. The bond lengths are given in Å (see left part) and the total charge of the displayed moiety (see right part) are indicated in bold. (B) Schematic $S_0$, $S_1$ and $S_2$ energy profiles along the $S_1$ PES path driving the chromophore $S_1$ isomerization. An $S_1$ PES dominated by a 1Bu character (left) is associated with a barrier-less path while a mixed 1Bu/2Ag character (right) is associated with the presence of a barrier along the path. The dashed energy profiles represent the energy of diabatic states corresponding to “pure” 1Bu and 2Ag electronic characters.

Author Manuscript

Author Manuscript

Author Manuscript

Author Manuscript

**Table 1.**

Time constants and amplitudes from the bi-exponential decay of SE, average ESLs, and experimentally determined fluorescence QYs (Φ) with respect to that of bacteriorhodopsin ($\Phi_{bR}$), determined from the spectrally integrated fluorescence intensities. See footnote [a].

| Sample | A1 | t1 (ps) | A2 | t2 (ps) | ESL (ps) | $\Phi/\Phi_{bR}$ |
|---|---|---|---|---|---|---|
| DA L83Q | 0.78 | 0.27±0.05 | 0.22 | 1.2±0.2 | 0.48 | 2.4 |
| DA WT | 0.72 | 0.55±0.05 | 0.28 | 1.7±0.2 | 0.86 | 1.1 |
| OA W76S/Y179F | 0.60 | 2.8±0.3 | 0.40 | 10±0.8 | 5.7 | 8.7 |
| GA W76S/Y179F | 0.40 | 2.1±0.4 | 0.60 | 8±0.7 | 5.7 | 7.6 |

[a]The fluorescence QY's are determined with bacteriorhodopsin as a reference sample (see SI). However, we refrain from quoting absolute values since the only available experimentally determined value for bacteriorhodopsin appears to be excessively high, most probably due to contributions from later photo-cycle intermediates.[34]